Inorganic−Organic Hybrid Coatings on Stainless Steel by Layer-by-Layer Deposition and Surface-Initiated Atom-Transfer-Radical Polymerization for Combating Biocorrosion

S. J. Yuan,[†] S. O. Pehkonen,[‡] Y. P. Ting,[†] K. G. Neoh,[†] and E. T. Kang*,[†]

Department of Chemical and Biomolecular Engineering, National University of Singapore, 10 Kent Ridge Crescent, Singapore 119260, Singapore, and CEWIC, Thule Institute, University of Oulu, P.O. Box 7300, Oulu FI-90014, Finland

ABSTRACT To improve the biocorrosion resistance of stainless steel (SS) and to confer the bactericidal function on its surface for inhibiting bacterial adhesion and biofilm formation, well-defined inorganic−organic hybrid coatings, consisting of the inner compact titanium oxide multilayers and outer dense poly(vinyl-*N*-hexylpyridinium) brushes, were successfully developed. Nanostructured titanium oxide multilayer coatings were first built up on the SS substrates via the layer-by-layer sol−gel deposition process. The trichlorosilane coupling agent, containing the alkyl halide atom-transfer-radical polymerization (ATRP) initiator, was subsequently immobilized on the titanium oxide coatings for surface-initiated ATRP of 4-vinylpyridine (4VP). The pyridium nitrogen moieties of the covalently immobilized 4VP polymer, or P(4VP), brushes were quaternized with hexyl bromide to produce a high concentration of quaternary ammonium salt on the SS surfaces. The excellent antibacterial efficiency of the grafted polycations, poly(vinyl-*N*-pyridinium bromide), was revealed by viable cell counts and atomic force microscopy images of the surface. The effectiveness of the hybrid coatings in corrosion protection was verified by the Tafel plot and electrochemical impedance spectroscopy measurements.

KEYWORDS: stainless steel • biocorrosion • inorganic−organic hybrid coatings • ATRP • layer-by-layer deposition

INTRODUCTION

Stainless steels (SSs) have been extensively used in industrial and marine environments because of their good corrosion resistance arising from a thin and compact chromium-enriched oxide layer (1). However, they are particularly susceptible to biocorrosion of sulfate-reducing bacteria (SRB) and to localized corrosion by chloride and reducing sulfur compounds (2, 3). The role of SRB in biocorrosion is well established, and enhanced corrosion is mainly attributed to cathodic depolarization (4), production of aggressive sulfide ions (5), binding of metal ions by extracellular polymeric substances (6), and formation of ferrous sulfide (7). Biocorrosion is becoming an important issue in marine and industrial environments because at least 20 % of all corrosion is associated with biocorrosion, at a direct cost of $30−50 billion annually (8). It is, therefore, of great importance to mitigate biocorrosion to prolong the service life of maritime structures and equipment.

Various strategies have been developed to address the growing need for combating biocorrosion (9−11). The conventional biocidal treatment is accompanied by environmental risks and is more difficult to implement in open systems, such as in marine environments (9). Protective antifouling coatings, such as tributyltin-based paints, are alternative means to alleviate the problems of biofouling and biocorrosion in seawater environments (10). Although effective, their applications have been banned by the International Maritime Organization since 2003 because the release of toxic metal ions, such as tin and copper, from the paint matrix is detrimental to nontargeted marine organisms (11). In view of the complicated environmental, ecological, and economical issues, more recent efforts are focused on developing environmentally benign antimicrobial coatings to prevent bacterial adhesion and biofilm formation (12−20). The formation of biofilms has been widely recognized as the key step in initiating biocorrosion. Inorganic−organic hybrid coatings have received considerable attention in corrosion protection (21−23). The organic component can provide flexibility and functional compatibility, while the inorganic component can provide enhanced scratch resistance, mechanical strength, durability, and adhesion to the metal surface (24). The inorganic−organic hybrid composites are usually prepared via a sol−gel process (25−27). Recent developments in controlled/"living" radical polymerization have provided an alternative approach for introducing well-defined polymer and copolymer brushes to a variety of inorganic substrates in the preparation of inorganic−organic hybrids (28).

In our previous study, nanostructured titanium oxide coatings prepared by the layer-by-layer (LBL) sol−gel deposition process on SS surfaces were shown to provide good
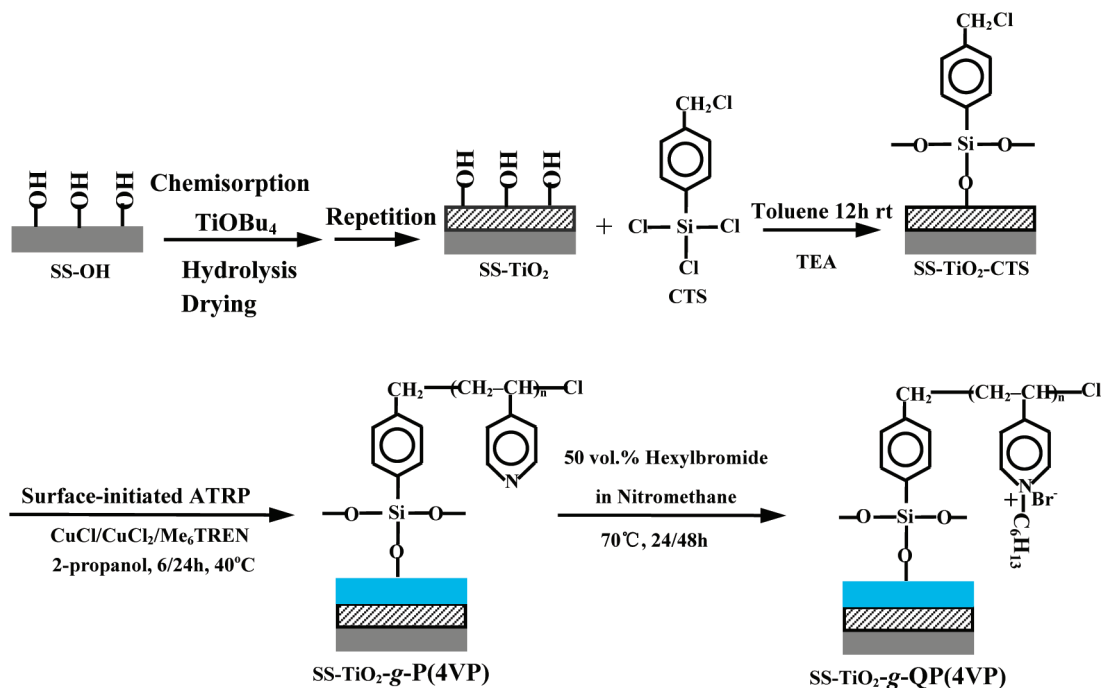

FIGURE 1. Schematic diagram illustrating the processes of formation of titanium oxide multilayers on the SS-OH surface via LBL sol−gel deposition (the SS-TiO$_2$ surface), coupling of CTS to the SS-TiO$_2$ surface (the SS-TiO$_2$-CTS surface), surface-initiated ATRP of 4VP to form the SS-TiO$_2$-g-P(4VP) surface, and subsequent quaternization of the SS-TiO$_2$-g-P(4VP) surface into the antibacterial SS-TiO$_2$-g-QP(4VP) surface.

corrosion-protective, as well as bioactive, properties (29). Nevertheless, the titanium oxide coatings have also been found to be susceptible to biofouling. To circumvent this problem, well-structured inorganic−organic hybrid coatings, prepared from LBL sol−gel deposition of the titanium oxide layer, followed by surface-initiated atom-transfer-radical polymerization (ATRP), were developed to confer both anticorrosion and antibacterial properties to the SS surface to further improve the biocorrosion resistance of SS in aggressive environments. Figure 1 depicts schematically the process of preparing inorganic−organic hybrid coatings on a SS surface. Nanostructured titanium oxide multilayers are first established on the SS surface via the LBL sol−gel deposition process. Subsequently, a trichlorosilane coupling agent, containing the alkyl halide ATRP initiator, is immobilized on the titanium oxide-coated surface for surface-initiated ATRP of 4-vinylpyridine (4VP). The tertiary amino groups of the grafted poly(4-vinylpyridine), or P(4VP), brushes are finally quaternized with hexyl bromide to produce the biocidal quaternary ammonium compounds. Positively charged quaternary ammonium groups can interact with the phospholipids bilayer of the cell membrane and disrupt its integrity, leading to leakage of intercellular components and subsequent cell death (16, 19). The antibacterial and anticorrosion properties of the inorganic−organic hybrid coatings were evaluated respectively by bactericidal assays and electrochemical analyses.

MATERIALS AND METHODS

Materials. Type 304 stainless steel (3 mm in thickness, nominal composition of 71.376% Fe, 8.18% Ni, 0.053% C, 18.08% Cr, 0.06% Cu, 1.68% Mn, 0.05% Mo, 0.047% N, 0.037% P, 0.007% S, and 0.43% Si) was purchased from Metal

Samples Co. (Munford, AL). Titanium(IV) butoxide (97%), 4-[(chloromethyl)phenyl]trichlorosilane (CTS; 97%), hexyl bromide (98%), copper(I) chloride (99%), copper(II) chloride (97%), and a H$_2$O$_2$ solution (30%) were obtained from Sigma-Aldrich Chemical Co. (St. Louis, MO) and used as received. Solvents, such as ethanol, toluene, acetone, triethanolamine (TEA), and methanol, and sulfuric acid (95−98%) were used as received. Tetrahydrofuran (THF; reagent grade) and 2-propanol (reagent grade) were obtained from Fisher Scientific Co. (Leics, U.K.). 4-Vinylpyridine (4VP; 97%) was obtained from Sigma-Aldrich Chemical Co., distilled under reduced pressure, and then stored under an argon atmosphere at −10 °C. Tris[2-(dimethylamino)ethyl]amine (Me$_6$TREN) was synthesized following the procedures reported previously (30). Yeast extract and agar were purchased from Oxoid Ltd. (Hampshire, U.K.). The sulfate-reducing bacterium of *Desulfovibrio desulfuricans* (ATCC, No. 27774) was obtained from American type Culture Collection. Phosphate buffer solution (PBS; containing NaH$_2$PO$_4$ of 4.68 g/L and Na$_2$HPO$_4$ of 8.662 g/L) was prepared afresh and sterilized in an autoclave before use.

Metal Coupon Preparation and Titanium Oxide Multilayer Coatings. The 3-mm-thick SS plates were ground sequentially with up to 1200-grit SiC paper and cut into coupons of about 10 mm × 10 mm in area. These coupons were further polished to a mirror-finish surface with an alumina suspension (about 0.3 μm in particle size). The newly polished coupons were washed with deionized water, acetone, ethanol, and deionized water, in that order, for 5 min each to degrease and clean the surface. The clean coupons were treated with a Piranha solution to generate a hydroxyl-enriched, or a hydroxylated, surface (SS-OH surface). Details on the preparation and characterization of the SS-OH surface have been described previously (29, 31).

The nanostructured titanium oxide multilayer coatings were deposited on the SS-OH surface using the LBL sol−gel deposition process described previously (32). Briefly, the SS-OH coupons were immersed in a 100 mM toluene/ethanol (1:1, v/v) solution of titanium(IV) butoxide for 10 min in a sealed Pyrex tube. The solution was purged a priori with purified argon for 30 min. Titanium(IV) butoxide reacted readily with the hydroxyl
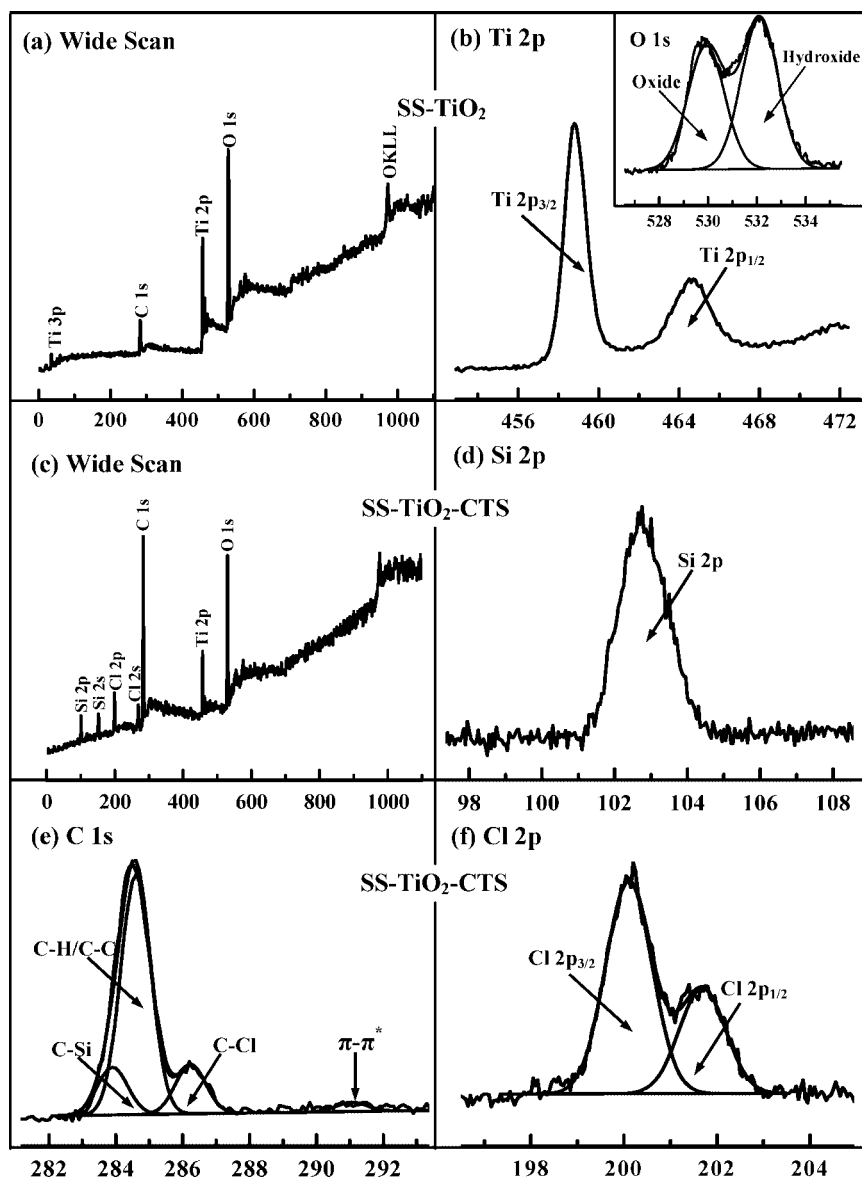
FIGURE 2. (a and b) Wide-scan and Ti 2p core-level spectra of the SS-TiO$_2$ surface. (c−f) Wide-scan and Si 2p, C 1s, and Cl 2p core-level spectra of the SS-TiO$_2$-CTS surface.

groups of the SS-OH surface in self-assembly. After rinsing with copious amounts of toluene to remove the unbound alkoxides, the coupons were immersed in deionized water for 2 min to regenerate the hydroxyl groups (Ti-OH), followed by drying in an air stream. The chemisorptions, rinsing, hydrolysis, and drying steps were repeated five times to produce the titanium oxide-coated, or SS-TiO$_2$, coupons. The SS-TiO$_2$ coupons were stored in a vacuum desiccator for further functionalization.

Immobilization of the Initiator on the SS-TiO$_2$ Surface. The silane coupling agent, CTS, was immobilized on the SS-TiO$_2$ surface via self-assembly. The SS-TiO$_2$ coupons were immersed in 8 mL of an anhydrous toluene solution, containing 0.28 mL of TEA (2×10^{-3} mol) and 0.2 mL of CTS (10^{-3} mol), for 12 h at room temperature. The coupons were subsequently removed and washed ultrasonically with copious amounts of chloroform, acetone, methanol, and finally deionized water, in that order. The silane-coupled SS-TiO$_2$ substrates, or SS-TiO$_2$-CTS substrates, containing the alkyl halide ATRP initiator, were then stored in a vacuum desiccator after being dried under reduced pressure.

Surface-Initiated ATRP of 4VP and Quaternization by Hexyl Bromide. Surface-initiated ATRP of 4VP from the SS-

TiO$_2$-CTS surface was accomplished in a Pyrex tube by immersing the SS-TiO$_2$-CTS coupon into the reaction mixture containing 3.0 mL of 4VP (27.8 mmol), 27.7 mg of CuCl (0.278 mmol), 7.51 mg of CuCl$_2$ (0.056 mmol), 120 μL of Me$_6$TREN, and 3 mL of 2-propanol. The suspension was purged with argon for about 30 min to remove the dissolved oxygen. The tube was then sealed. The polymerization reactions were carried out at 40 °C for 6 and 24 h to produce two different SS-TiO$_2$-g-P(4VP) surfaces. At the end of each polymerization reaction, the P(4VP)-grafted coupons were washed exhaustively with 2-propanol, methanol, and deionized water to remove the unreacted monomer and residual homopolymer. They were then dried in a vacuum desiccator. The SS-TiO$_2$-g-P(4VP) surface from 24 h of ATRP was further exposed to 10 mL of a 50% nitromethane solution of hexyl bromide to convert the pyridine nitrogen moieties into the pyridinium cationic groups via N-alkylation. The quaternization reaction was carried out at 70 °C for either 24 or 48 h to produce the SS-TiO$_2$-g-QP(4VP) surfaces. After the quaternization reaction, the coupons were rinsed with THF and methanol to remove the unreacted alkyl halide, prior to being dried in a vacuum desiccator.

Table 1. Static Water Contact Angles (deg) of Different Substrate Surfaces

sample surface	static water contact angles
pristine SS[a]	56
SS-OH[b]	18
SS-TiO$_2$[c]	29
SS-TiO$_2$-CTS[d]	93
SS-TiO$_2$-g-P(4VP)[e]	90
SS-TiO$_2$-g-P(4VP)[f]	76
SS-TiO$_2$-g-QP(4VP)[g]	37

[a] Pristine SS corresponds to a newly polished SS coupon. [b] SS-OH was obtained after the pristine SS coupon was treated in the Piranha solution for 30 min. [c] SS-TiO$_2$ corresponds to the hydrolyzed titanium oxide/butoxide-coated coupon obtained via the fifth cycle of the LBL sol−gel deposition process. [d] SS-TiO$_2$-CTS corresponds to the SS-TiO$_2$ coupon silanized with CTS. The thickness of the silane layer was ∼0.4 nm. [e] Reaction conditions: [4VP]:[CuCl]:[CuCl$_2$]:[Me$_6$TREN] = 100:1.0:0.2:1.5 in 2-propanol/4VP (1:1, v/v) at 40 °C for 6 h. [f] Reaction conditions: [4VP]:[CuCl]:[CuCl$_2$]:[Me$_6$TREN] = 100:1.0: 0.2:1.5 in 2-propanol/4VP (1:1, v/v) at 40 °C for 24 h. [g] SS-TiO$_2$-g-QP(4VP) refers to the SS-g-P(4VP) surface from 24 h of ATRP after quaternization with hexyl bromide for 48 h.

Surface Characterization. The composition of surface-functionalized substrates was determined by X-ray photoelectron spectroscopy (XPS). The XPS measurements were performed on a Kratos AXIS HSi spectrometer with an Al Kα X-ray source (1486.6 eV photons), using procedures similar to those described previously (29). The topography of the functionalized SS surfaces was studied by atomic force microscopy (AFM), using a Nanoscope IIIa AFM system and procedures similar to those described earlier (13). The arithmetic mean of the surface roughness (R_a) was calculated from the roughness profile determined by AFM. Static water contact angles of various substrate surfaces were measured at 25 °C and 60% relative humidity using the sessile drop method with a 3 μL water droplet and a telescopic goniometer [model 100-00-(230), Rame-Hart, Inc., Mountain Lake, NJ] (19). The telescope with a magnification power of 23× was equipped with a protractor of 1° graduation. For each angle reported, at least three measurements from different surface locations were averaged. The angles reported were accurate to ±3°.

Microorganism Cultivation and Inoculation. Gram-negative *D. desulfuricans* (ATCC, No. 27774) bacterium was cultured in the simulated seawater-based modified Baar's (SSMB) medium using procedures similar to those described previously (29). Each 1 L of the SSMB medium contained 23.476 g of NaCl, 3.917 g of Na$_2$SO$_4$, 0.192 g of NaHCO$_3$, 0.664 g of KCl, 0.096 g of KBr, 10.61 g of MgCl$_2$ · 6H$_2$O, 1.469 g of CaCl$_2$ · 6H$_2$O, 0.026 g of H$_3$BO$_3$, 0.04 g of SrCl$_2$ · 6H$_2$O, 0.41 g of MgSO$_4$ · 7H$_2$O, 0.1 g of NH$_4$Cl, 0.1 g of CaSO$_4$, 0.05 g of K$_2$HPO$_4$, 0.1 g of (NH$_4$)$_2$Fe(SO$_4$)$_2$, 0.5 g of trisodium citrate, 3.5 g of sodium lactate, and 1.0 g of yeast extract. The pH of the medium was adjusted to 7.5 ± 0.1 using a 5 M NaOH solution. The medium was then sterilized by autoclaving at 121 °C for 20 min.

For the inoculation medium, a 1-mL aliquot of the 3-day-old *D. desulfuricans* was introduced into 500 mL of the SSMB medium in a Scott Duran bottle (1.0 L). The medium was incubated at 30 °C in an anaerobic workstation (Don Whitley, model MASC MG 500, Maharashtra, India) and maintained in an atmosphere containing 5% H$_2$, 5% CO$_2$, and 90% N$_2$. The bacteria cell counts were determined using the three-tube most probable number (MPN) method (1). The pristine and surface-functionalized coupons were sterilized in a 70% ethanol solution for 8 h and dried by purging with pure N$_2$. When the density of *D. desulfuricans* increased to more than 10^6 MPN/mL after 2 days of incubation, these coupons were aseptically introduced into the medium to determine antibacterial and corrosion-

protective properties of the SS-TiO$_2$-g-QP(4VP) surface. The planktonic viable cell density of *D. desulfuricans* in the bulk medium remained in the range of 10^6−10^8 MPN/mL, with the biogenic sulfide ions in the range of 30−40 mg/L (about 0.94−1.25 mM) in the present study, similar to those reported previously (29).

Adhesion and Viability Assay of the Surface-Functionalized Coupons. The ability of the inorganic−organic hybrid coatings to inhibit bacterial adhesion and proliferation was revealed by AFM imaging. The sample fixation and preparation for AFM imaging was as follows (19). The coupons were first washed with sterile PBS immediately after the exposure periods, followed by immersing in 3 vol % glutaradehyde (GA) PBS for 4 h at −4 °C to fix the bacteria cells. The substrates were removed from the GA solution and washed with PBS, followed by step dehydration with 25%, 50%, 70%, 95%, and 100% ethanol for 5 min each. The substrates were then dried and mounted on standard sample studs for AFM imaging.

The bactericidal properties of the inorganic−organic hybrid coatings were determined in a more quantitative manner by enumerating the viable cell counts on the substrate surface. The viable cells adhered on the pristine and surface-functionalized coupons were determined by the three-tube MPN method (1). At the end of a predetermined exposure period, the coupons were removed from the culture medium and then introduced into 10 mL of sterile PBS, followed by sonication in an ultrasonic bath for 3 min at a frequency of 40−50 kHz. Serial dilutions with PBS were repeated with each initial bacterial suspension. A total of 1 mL of each diluted suspension was inoculated in triplicate in separate tubes containing 9 mL of the culture medium. After 72 h of incubation at 30 °C, the broth from each tube was examined for the presence or absence of bacterial growth. The results, after accounting for the dilution factor, were expressed as mean viable cell counts for each substrate.

Electrochemical Analyses of the Surface-Functionalized Coupons. The corrosion-inhibition properties of inorganic−organic hybrid coatings on the SS surface were evaluated by measurement of the Tafel plots and impedance spectra using an Autolab PGSTAT 30 (EcoChemie, Utrecht, The Netherlands) electrochemical workstation. The experimental procedures for the electrochemical studies were similar to those described previously (29). Briefly, the coupons were removed from the culture medium after the prescribed exposure time. They were then embedded in a poly(vinylidene difluoride) holder to leave an exposed surface area of 0.785 cm^2 and mounted as the working electrode in a three-electrode glass corrosion cell. A platinum rod was used as the counter electrode and an Ag/AgCl electrode as the reference electrode. Tafel plots were obtained at a scan rate of 2 mV/s in the range of −250 to +250 mV versus the open-circuit potential (OCP). The impedance spectra were recorded at 7 points per decade under OCP using a 10-mV amplitude sinusoidal signal in the frequency range of 0.005−100 000 Hz. The inhibition efficiency (IE) of the surface-functionalized coupons was calculated using the following equation (13):

$$\text{IE \%} = \frac{i_o - i_{corr}}{i_o} \qquad (1)$$

wherein i_o and i_{corr} are the corrosion current densities of the pristine and surface-functionalized coupons, respectively, as determined by analysis of the Tafel plots.

RESULTS AND DISCUSSION

Deposition of Titanium Oxide Multilayer Coatings on the SS Substrate. A Piranha solution, as a strong oxidizer, has been known to generate an oxidized/hydroxy-
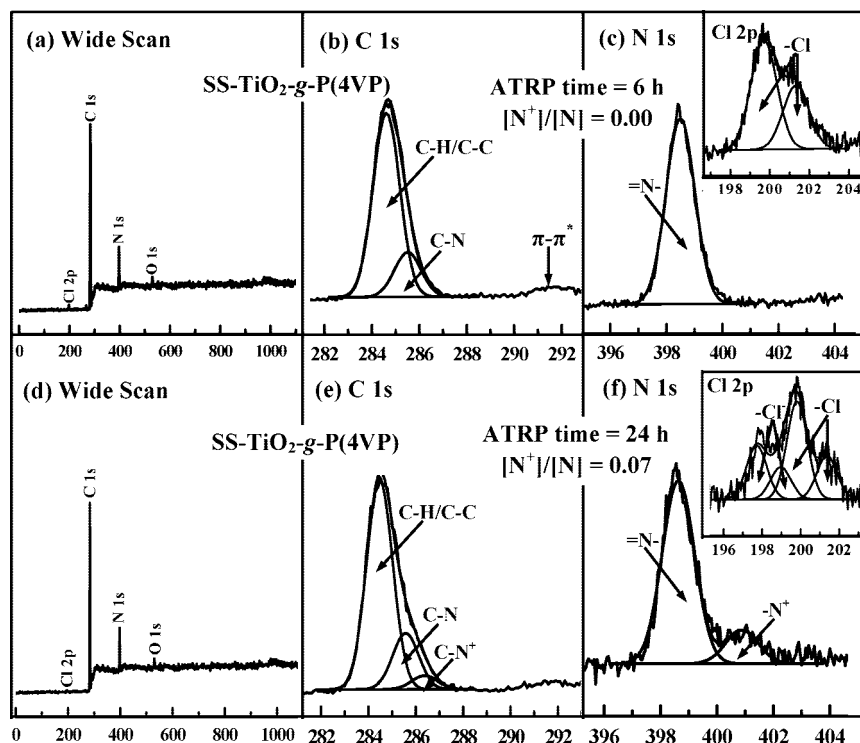
FIGURE 3. Wide-scan and C 1s, N 1s, and Cl 2p core-level spectra of the (a–c) SS-TiO$_2$-g-P(4VP) surface from 6 h of ATRP and (c–e) SS-TiO$_2$-g-P(4VP) surface from 24 h of ATRP.
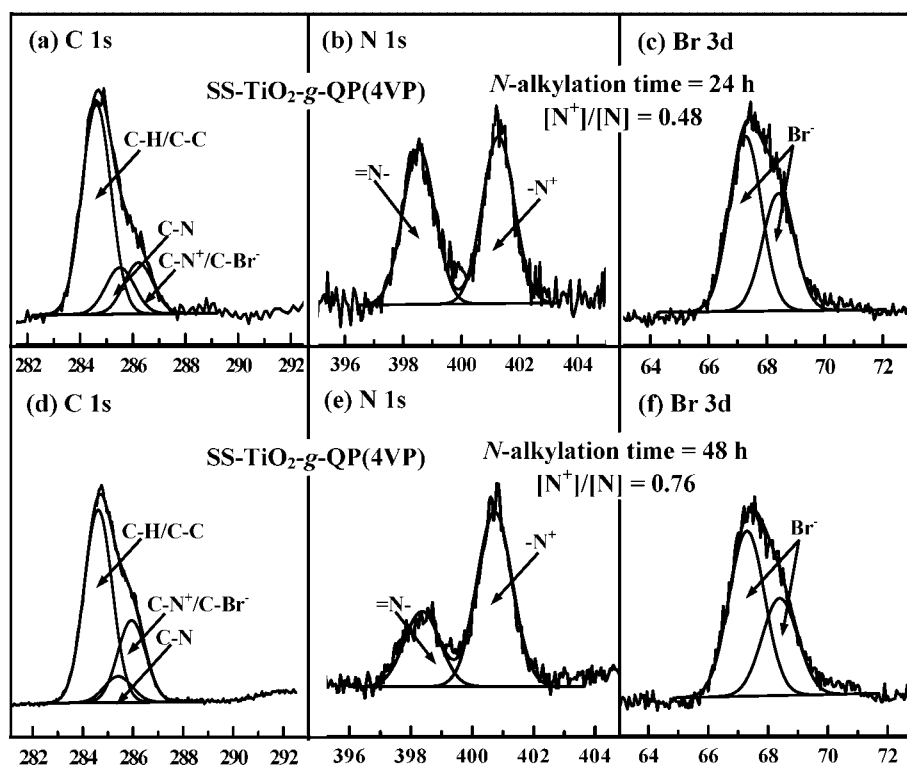

FIGURE 4. C 1s, N 1s, and Br 3d core-level spectra of (a–c) the SS-TiO$_2$-g-QP(4VP) surface from 24 h of quaternization reaction and (d–f) the SS-TiO$_2$-g-QP(4VP) surface from 48 h of quaternization reaction.

lated surface on most metals (29, 31). The chemical composition of the hydoxylated SS, or the SS-OH surface, after the Piranha treatment has been determined by XPS, as described in a previous study (29). The enrichment of hydroxyl (−OH) groups produces a more hydrophilic SS surface, as the static water contact angle of the surface

decreases from about 56° to about 18°. The successful deposition of titanium oxide multilayer coatings on the SS-OH substrate via LBL deposition was ascertained by XPS and static water contact angle measurements. Parts a and b of Figure 2 show the respective wide scan and Ti 2p core-level spectra of the Ti-OH-deposited SS-OH, or the SS-TiO$_2$, sur-
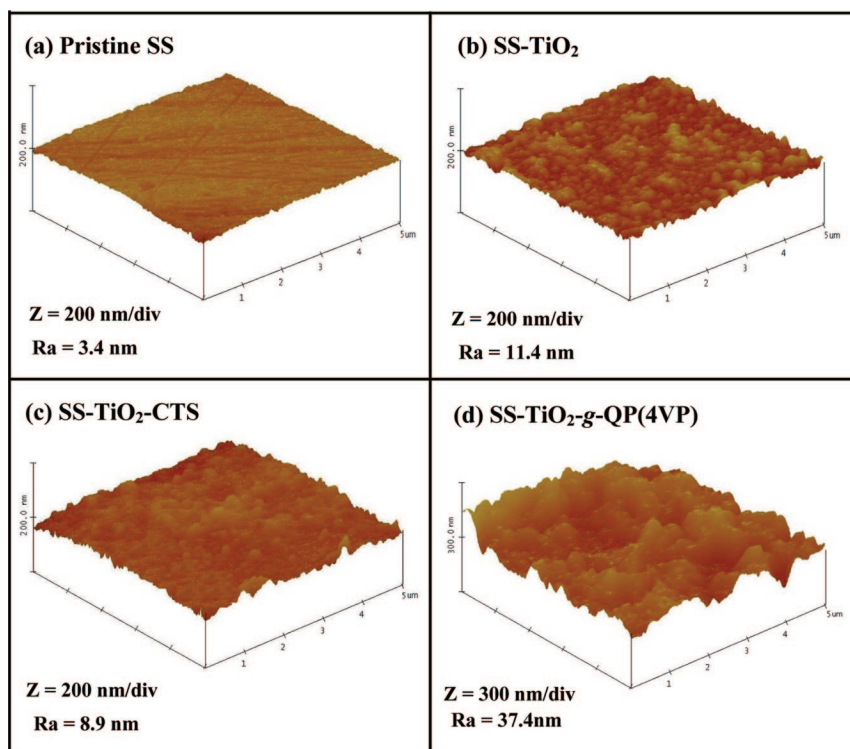
FIGURE 5. AFM images of the (a) pristine SS, (b) SS-TiO$_2$, (c) SS-TiO$_2$-CTS, and (d) SS-TiO$_2$-*g*-QP(4VP) surfaces (scan size: 5 μm $\times$ 5 μm).

face. The wide-scan spectrum of the SS-TiO$_2$ surface is dominated by signals attributable to Ti, O, and C (Figure 2a). The C signal was probably associated with hydrocarbon contamination for samples exposed to the ambient atmosphere or with a small amount of nonhydrolyzed butoxides (33). The masking of Fe and Cr signals on the SS-TiO$_2$ coupons implies that the titanium oxide multilayer coating is thicker than the probing depth of the XPS technique (about 8 nm) (34). The thickness of a five-layer titanium oxide coating has been reported to be about 22 nm in a previous study (35). The Ti 2p spectrum shows a spin−orbit split doublet with binding energies (BEs) of 458.8 and 464.3 eV, attributable to the respective Ti 2p$_{3/2}$ and Ti 2p$_{1/2}$ peak components of the TiO$_2$ layer (Figure 2b) (33), consistent with the previous finding that the titanium oxide prepared by the sol−gel process is predominantly in the form of titanium(IV) oxides and a small amount of nonstoichiometric Ti$_x$O$_y$ (35). The corresponding O 1s core-level spectrum of the surface shows two predominant peak components at BEs of 529.9 and 531.7 eV, attributed to oxide and hydroxide species, respectively (inset of Figure 2b) (33). The SS-TiO$_2$ surface has a small static water contact angle of about 29° (Table 1).

Immobilization of the ATRP Initiator on the SS-TiO$_2$ Surface. The TEA-catalyzed silanization of the SS-TiO$_2$ surface with CTS provides not only a dense silane passivation layer but also initiation sites for surface-initiated ATRP. As compared to that of the SS-TiO$_2$ surface (Figure 2a), the appearance of additional Cl and Si signals in the wide-scan spectrum (Figure 2c) is consistent with the presence of a coupled halide-containing silane layer on the SS-TiO$_2$ surface (SS-TiO$_2$-Cl surface). The persistence of the Ti

signal indicates that the silane layer is thinner than the probing depth of the XPS technique (about 8 nm) (34). The thickness of the silane layer has been reported to be about 0.4 nm (36). The [Si]/[C]/[Cl] ratio, as determined from the Si 2p, C 1s, and Cl 2p core-level spectral area ratio (Figure 2d−f), is about 1.0:7.1:1.1, which is comparable to that of the theoretical value of 1:7:1 for CTS. The C 1s core-level spectrum is curve-fitted into three peak components with BEs at 283.9, 284.6, and 286.2 eV, attributable to the C−Si, C−C/C−H, and C−Cl species (33), respectively (Figure 2e). The area ratio of the three peak components is 1.0:5.1:1.1, which is comparable to the theoretical value of 1:5:1 for CTS. The π−π* shakeup satellite associated with the aromatic ring of CTS is also discernible at a BE of about 291 eV. The increase in the static water contact angle of the surface from about 29° to 93° (Table 1) is also consistent with the successful immobilization of CTS on the SS-TiO$_2$ surface. The Cl 2p core-level spectrum consists of a spin−orbit split doublet, with the Cl 2p$_{3/2}$ and Cl 2p$_{1/2}$ peak components located at BEs of about 200 and 201.6 eV, respectively, attributable to the covalent chloride species (19) of the benzyl chloride moiety of the immobilized silane (Figure 2f). Thus, the benzyl chloride groups have been successfully immobilized on the SS-TiO$_2$-CTS surface to cater to the subsequent surface-initiated ATRP of 4VP.

Surface-Initiated ATRP of 4VP and Quaternization by Hexyl Bromide. In this study, the molar ratio of [4VP (monomer)]/[CuCl (catalyst)]/[CuCl$_2$ (deactivator)]/ [Me$_6$TREN (ligand)] was controlled at 100:1:0.2:1 to produce the SS-TiO$_2$-*g*-P(4VP) surfaces. Parts a−c of Figure 3 and the inset of Figure 3c show the respective wide-scan and C 1s, N 1s, and Cl 2p core-level spectra of the SS-TiO$_2$-*g*-P(4VP)
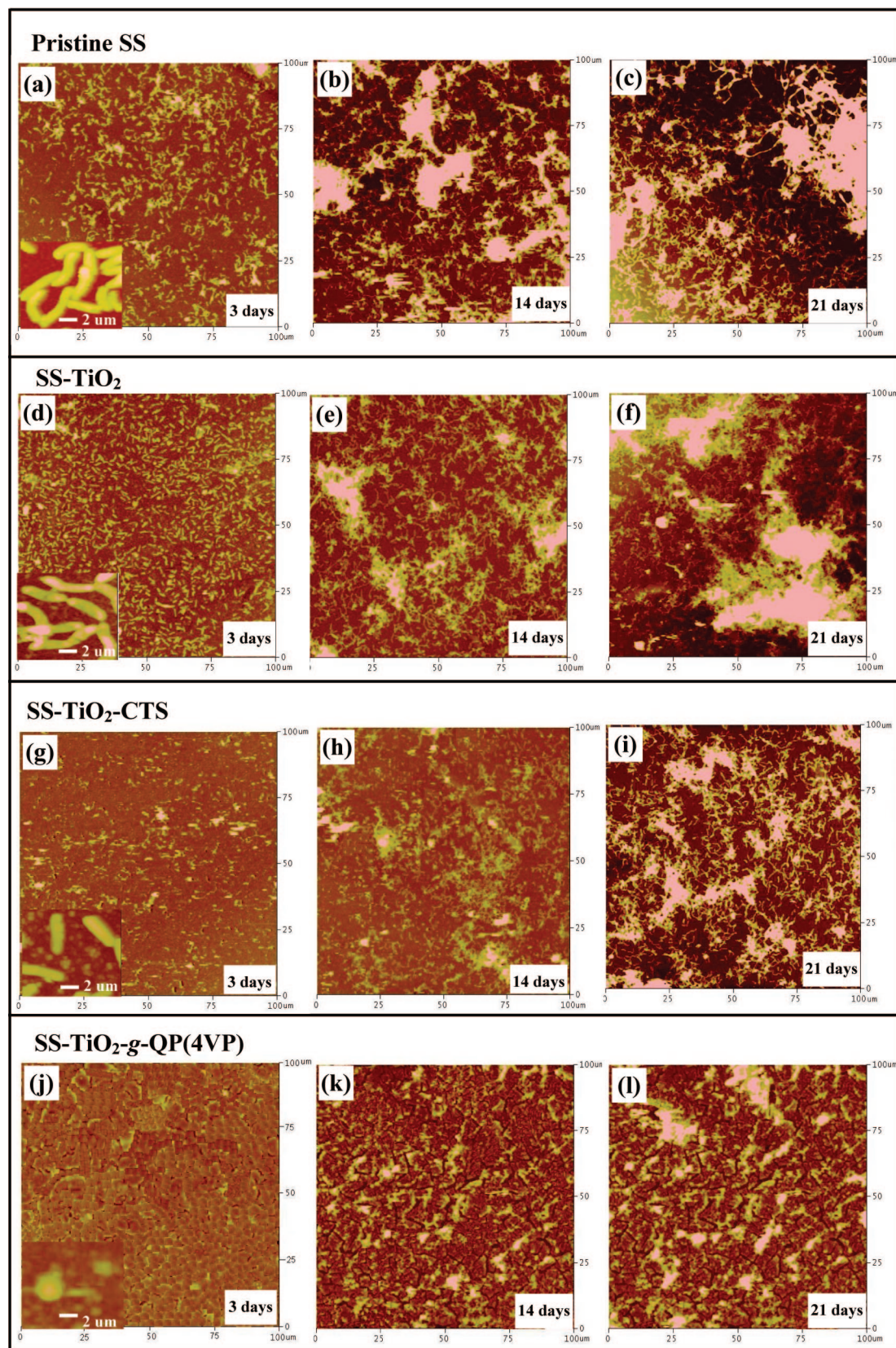
FIGURE 6. Representative AFM images of (a−c) the pristine, (d−f,) the SS-TiO$_2$, (g−i) the SS-TiO$_2$-CTS, and (j−l) the SS-TiO$_2$-*g*-QP(4VP) surfaces after 3, 14, and 21 days of exposure in the *D. desulfuricans* inoculated SSMB medium (scan size: 100 μm × 100 μm).

surface from 6 h of ATRP. The disappearance of the Ti and Si signals and the appearance of the N signals in the wide-scan spectrum of the SS-TiO$_2$-*g*-P(4VP) surface indicates that

the thickness of the P(4VP) brushes is larger than the probing depth of the XPS technique (about 8 nm (34)) after 6 h of ATRP (Figure 3a). The surface [N]/[C] ratio of about 0.13, as
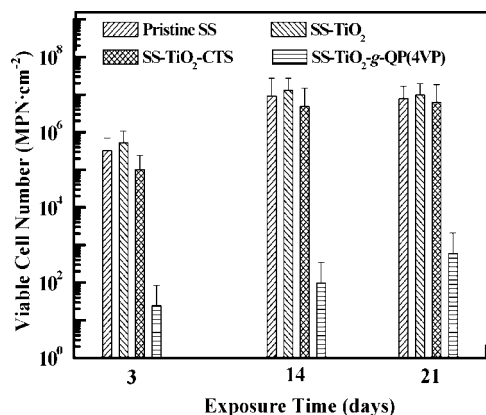
FIGURE 7. Number of viable *D. desulfuricans* cells attached to the pristine, the SS-TiO₂, the SS-TiO₂-CTS, and the SS-TiO₂-*g*-QP(4VP) surfaces as a function of the exposure time in the *D. desulfuricans* inoculated SSMB medium.

determined from the sensitivity-factor-corrected N 1s and C 1s spectral area ratio, is fairly close to the theoretical value of 0.14 expected for P(4VP). The C 1s core-level spectrum shows two peak components with BEs at about 284.6 and 285.5 eV, attributable to the C—H/C—C and C—N species (33, 37), respectively, as well as the $\boldsymbol{\pi-\pi}^*$ shakeup satellite at a BE of about 291 eV, associated with the aromatic pyridine ring (Figure 3b). The N 1s core-level spectrum shows predominantly a peak component at a BE of 398.5 eV, attributable to the imine moiety of the pyridine rings (Figure 3c) (37). The persistence of Cl species (Cl $2p_{3/2}$ and Cl $2p_{1/2}$ doublet; see the inset of Figure 3c) is consistent with the fact that the "living" chain end from the ATRP process involves a dormant alkyl halide group.

Parts d—f of Figure 3 and the inset of Figure 3f show the respective wide-scan and C 1s, N 1s, and Cl 2p core-level spectra of the SS-TiO₂-*g*-P(4VP) surface from 24 h of ATRP. The N 1s core-level spectrum of the SS-TiO₂-*g*-P(4VP) surface shows an additional minor peak component at a BE of about 401.5 eV, attributable to the positively charged nitrogen (N⁺) species (33) (Figure 3f), indicative of a small degree (about 7%) of quaternaization of the P(4VP) chains by the dormant alkyl halide groups at the chain ends from the ATRP process upon prolonging of the ATRP reaction time (38, 39). The self-quaternization effect is further confirmed by the appearance of an anionic chloride species (Cl⁻, with a Cl $2p_{3/2}$ BE at about 197 eV (19)) in the Cl 2p core-level spectrum (inset of Figure 3f). The appearance of an additional peak component at a BE of about 286.2 eV in the C 1s core-level spectrum, attributable to C—N⁺ species, is consistent with the partial quaternization of the P(4VP) chains (Figure 3e). The slight decrease in the static water contact angle (from about 90° to about 76°) of the SS-TiO₂-*g*-P(4VP) surface from 24 h of ATRP, as compared to that of the SS-TiO₂-*g*-P(4VP) surface from 6 h of ATRP, further confirms the partial quaternization of the P(4VP) chains (Table 1). It has been reported that the surface-initiated ATRP is strongly dependent on the reaction time and the length of the grafted polymer chains increases linearly with the polymerization time (39). However, the molecular weight and molecular weight distribution of the surface-grafted polymer cannot be determined with ac-
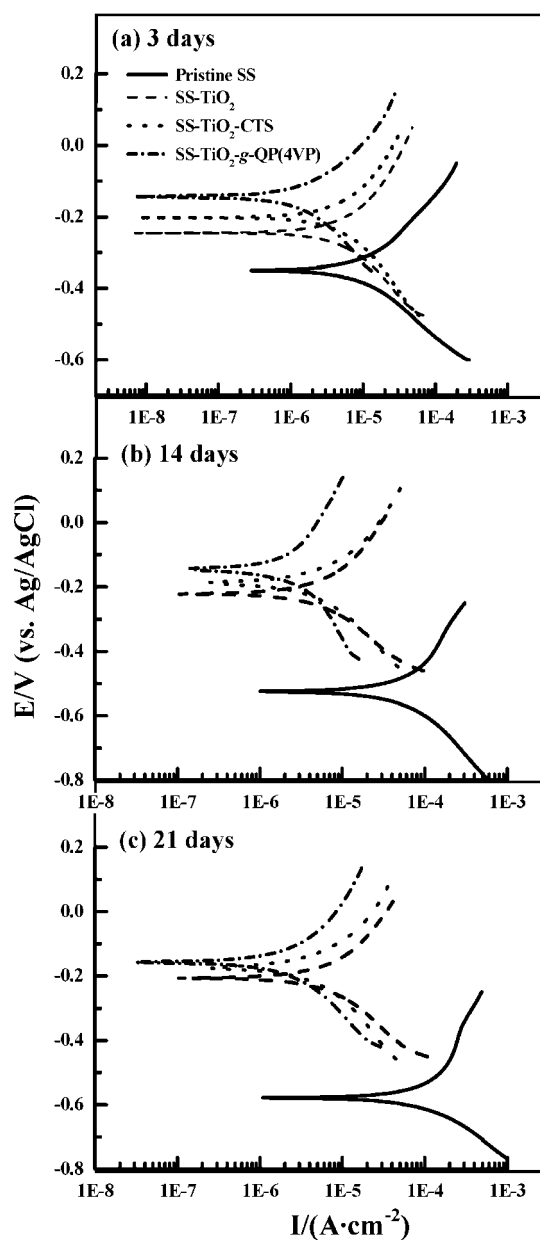

FIGURE 8. Tafel plots of the pristine SS, the SS-TiO₂, the SS-TiO₂-CTS, and the SS-TiO₂-*g*-QP(4VP) coupons after exposure to the *D. desulfuricans* inoculated SSMB medium for (a) 3, (b) 14, and (c) 21 days. The solid, dashed, dotted, and dash-dotted lines correspond to the pristine SS, SS-TiO₂, SS-TiO₂-CTS, and the SS-TiO₂-*g*-QP(4VP) coupons, respectively.

curacy without cleavage of a sufficient quantity of grafted chains. The amount of grafted polymer on the planar surface is minute. Only about 0.01 mg of the polymer can be obtained from a 100-nm-thick film grown on a 1-cm² surface (40). Thus, the quantity of polymers cleaved from the solid surface did not allow an accurate analysis of the molecular weight and molecular weight distribution by gel permeation chromatography (41, 42). The SS-TiO₂-*g*-P(4VP) surface from 24 h of ATRP with a thicker polymer film was used in the subsequent N-alkylation reaction to produce the antibacterial surface.

The imine moiety of pyridine rings was converted into the pyridinium cation by reaction with hexyl bromide to produce the biocidal effect. Parts a—c of Figure 4 show the

Table 2. Analysis of the Tafel Plots of Various Coupons as a Function of the Exposure Time in the *D. desulfuricans* Inoculated SSMB Medium

time (days)	sample	$b_a{}^a$ (mV/dec)	$b_c{}^b$ (mV/dec)	$E_{corr}{}^c$ (V)	i_{corr} (μA/cm^2)	IE^d (%)	corrosion rate (mm/year)
3	pristine SS	203	−178	−0.350	11.35		0.118
	SS-TiO$_2$	314	−226	−0.255	7.386	0.349	0.0765
	SS-TiO$_2$−CTS	260	−246	−0.187	5.963	0.475	0.0615
	SS-TiO$_2$-*g*-QP(4VP)	243	−218	−0.155	2.287	0.799	0.0237
14	pristine SS	401	−205	−0.526	77.32		0.800
	SS-TiO$_2$	310	−200	−0.226	6.753	0.913	0.0699
	SS-TiO$_2$−CTS	245	−263	−0.203	6.260	0.919	0.0626
	SS-TiO$_2$-*g*-QP(4VP)	289	−325	−0.168	2.348	0.971	0.0255
21	pristine SS	488	−181	−0.536	129.10		1.336
	SS-TiO$_2$	280	−218	−0.210	7.762	0.940	0.0803
	SS-TiO$_2$−CTS	285	−289	−0.194	7.332	0.943	0.0756
	SS-TiO$_2$-*g*-QP(4VP)	315	−248	−0.164	2.947	0.977	0.0305

^{a} b_a is the Tafel slope of the anodic polarization curve. ^{b} b_c is the Tafel slope of the cathodic polarization curve. ^{c} E_{corr} refers to the potential, where the current reaches zero under polarization. ^{d} IE denotes the inhibition efficiency.

respective C 1s, N 1s, and Br 3d core-level spectra of the SS-TiO$_2$-*g*-QP(4VP) surface after 24 h of N-alkylation reaction. The N 1s core-level spectra are curve-fitted into two peak components with BEs at about 398.5 and 401.5 eV, attributable to the neutral imine (−N$=$) and positively charged nitrogen (−N$^+$) species, respectively (Figure 4b) (33, 37). The [N$^+$]/[N] ratio is about 0.48 after 24 h of N-alkylation reaction, indicating that approximately half of the 4VP repeat units have been quaternized. The C 1s core-level spectra consist of three peak components with BEs at about 284.6, 285.5, and 286.2 eV, attributable to the C−H/C−C, C−N, and C−N$^+$/C−Br species (19, 33), respectively (Figure 4a). The [C−N$^+$]/[C−N] area ratio, as determined from the peak component area ratio of the curve-fitted C 1s core-level spectrum, is about 0.98 from 24 h of N-alkylation, in good agreement with the extent of quaternization deduced from the corresponding N 1s spectrum. The corresponding Br 3d core-level spectrum has a spin−orbit split doublet, Br 3d$_{5/2}$ and Br 3d$_{3/2}$, respectively, at BEs of 67.3 and 68.4 eV, attributable to the Br$^-$ species (19, 33). Upon prolonging of the quaternization reaction time to 48 h, the degree of N-alkylation of the pyridinium groups on the SS-TiO$_2$-*g*-QP(4VP) surface increases significantly. The [N$^+$]/[N] ratio has increased to about 0.76 (Figure 4e), while the corresponding ratio of the C−N$^+$ to C−N species in the C 1s core-level spectrum has also increased to about 3.2 (Figure 4d), indicating that about three-quarters of the P(4VP) repeat units have been converted into the pyridinium cations (N$^+$). The SS-TiO$_2$-*g*-QP(4VP) surface becomes more hydrophilic, in comparison with the starting SS-TiO$_2$-*g*-P(4VP) surface because the average static water contact angle has decreased to about 37° after 48 h of the N-alkylation reaction (Table 1). The SS-TiO$_2$-*g*-QP(4VP) coupons from 48 h of quaternization reaction were chosen for evaluation of the bactericidal and anticorrosion properties of the inorganic−organic hybrid coatings.

Surface Topography. The changes in topography of the SS surface after each functionalization step were investigated using AFM. Respective AFM images of the pristine and stepwise functionalized surfaces are shown in Figure 5. The pristine SS surface is fairly homogeneous and smooth, with a root-mean-square surface roughness (R_a) of about 3.4

nm (Figure 5a). The roughness of the SS-TiO$_2$ surface increases slightly to about 11.4 nm (Figure 5b), indicative of the formation of nanostructured titanium oxide multilyers via the LBL sol−gel deposition process. The chlorosilanization reaction probably has produced a uniform coverage of the halide initiator on the SS-TiO$_2$ surface because the R_a value remains at about 8.9 nm (Figure 5c). After the surface-initiated graft polymerization of 4VP and quaternization, the R_a value for the SS-TiO$_2$-*g*-QP(4VP) surface increased to about 37.4 nm (Figure 5d).

Adhesion and Viability Assay of Cells on the SS-TiO$_2$-*g*-QP(4VP) Coupons. AFM images were obtained for the various substrate surfaces from different exposure periods in the *D. desulfuricans* inoculated medium to assess the inhibitory effect of the inorganic−organic hybrid coatings to bacterial adhesion and proliferation. The respective AFM images are shown in Figure 6. Numerous bacteria cells, either individually or in small aggregates, were found to distribute randomly on the pristine SS coupon surface after 3 days of exposure (Figure 6a). Active cell growth and division are also discernible (inset of Figure 6a). Upon a prolonging of the exposure time, the pristine SS coupon surface is covered with dense, porous, and lumpy biofilms (Figure 6b,c). The porosity and discontinuity of biofilms have been reported to facilitate the localized attack by aggressive Cl$^-$ ions and biogenic S^{2-}, leading to the initiation of pitting or crevice corrosion (43). For the SS-TiO$_2$ coupons, bacterial colonization appears to have proceeded faster than that of the pristine SS coupon during the initial exposure periods (Figure 6d). This phenomenon is consistent with the earlier findings that bacterial adhesion occurs rapidly on titanium surfaces because titanium does not exhibit any toxicity toward most organisms (29, 44). The density of bacteria cells on the SS-TiO$_2$-CTS surface is lower than those on the corresponding pristine SS and the SS-TiO$_2$ coupons during the initial exposure periods (Figure 6g,h). Nevertheless, a thick and heterogeneous biofilm can also be observed on the SS-TiO$_2$-CTS surface after 21 days of exposure (Figure 6i). Thus, all of these surfaces are good templates for the proliferation of microorganisms and biofilm formation (45). Although factors governing cell adhesion are still obscure, the chemical and physiochemical nature of the
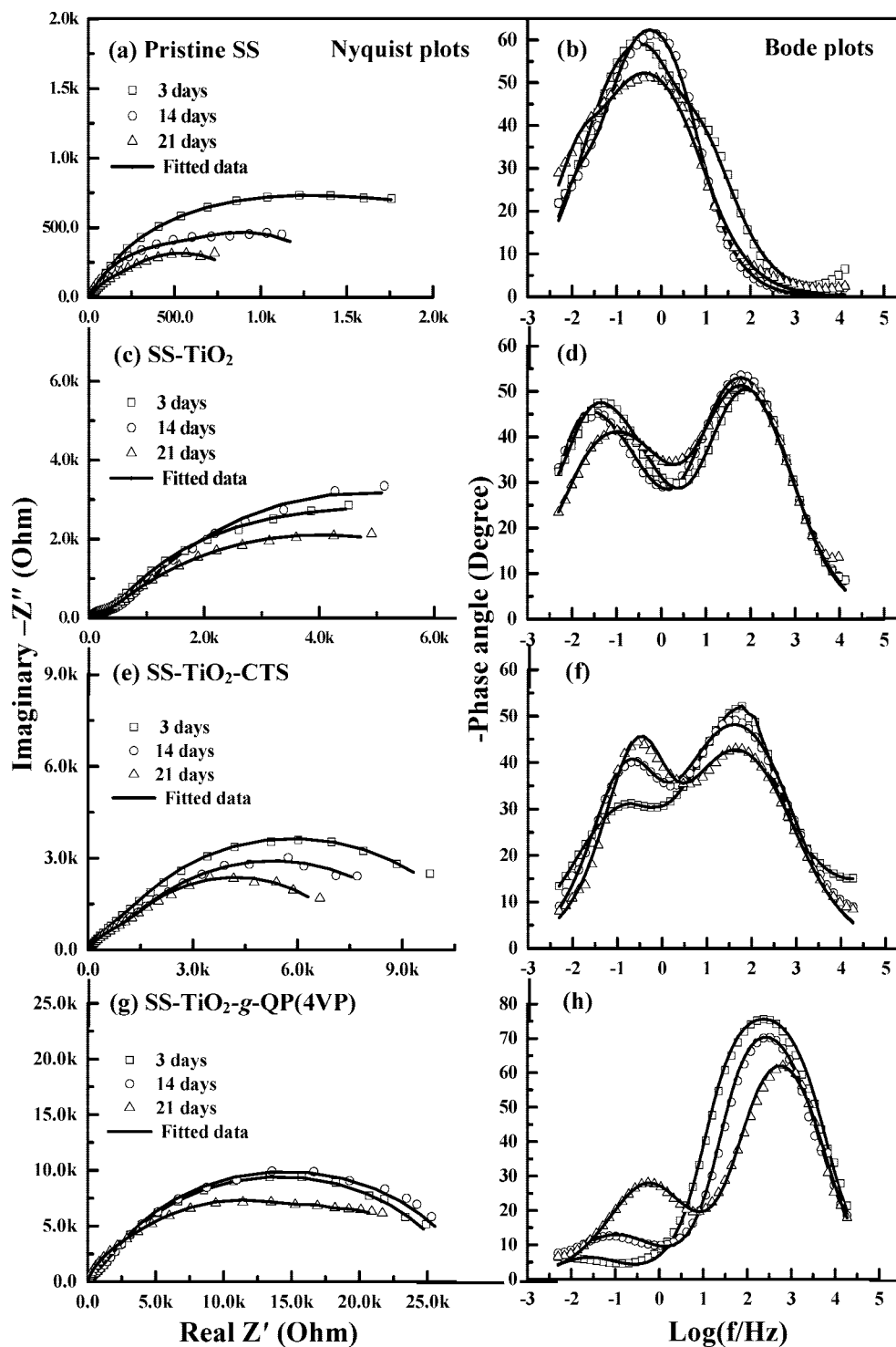
FIGURE 9. Impedance spectra of (a and b) the pristine SS, (c and d) the SS-TiO$_2$, (e and f) the SS-TiO$_2$-CTS, and (g and h) the SS-TiO$_2$-g-QP(4VP) coupons after exposure in the *D. desulfuricans* inoculated SSMB medium for 3, 7, and 21 days. The solid lines represent the fitted results based on the corresponding EECs.

substrates, such as hydrophobicity or hydrophilicity (46), steric hindrance (47), and roughness (48), and the existence of a "conditioning layer" at the substrate surface (49) are known to contribute to the initial cell attachment process.

In the case of the coupons with inorganic–organic hybrid coatings, bacterial adhesion is inhibited almost completely during the initial 3 days of exposure (Figure 6j). With an increase in the exposure time, some bacteria cells can be spotted over the SS-TiO$_2$-g-QP(4VP) surface. However, cell

aggregation and cell division are greatly reduced (Figure 6k,l). In contrast to cylindrically shaped bacteria cells with length ranging from 4 to 6 μm, as seen in the magnified images in the insets of parts a, d, and g of Figure 2, the bacteria cells on this surface are less than 2 μm in length and are deformed (inset of Figure 6j), suggesting that not only can the surface-bearing polycationic N$^+$ species inhibit the attachment of anaerobic *D. desulfuricans*, but they can also exhibit bactericidal effects (19). Most of the bacteria cells

Equivalent Circuits

(a)

$$R_s(Q_f[R_f(R_{ct}C_{dl})])$$

(b)

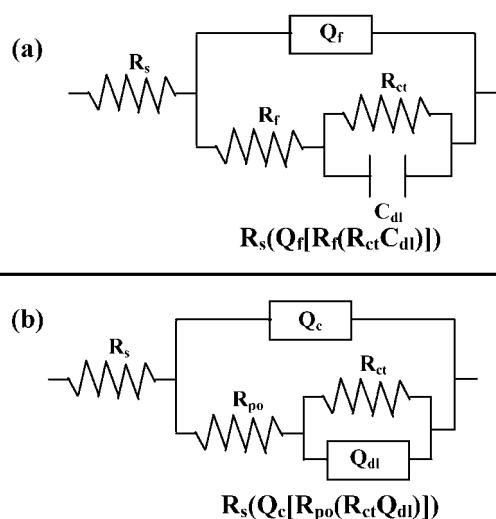$$R_s(Q_c[R_{po}(R_{ct}Q_{dl})])$$

FIGURE 10. EECs used for fitting of the impedance spectra of (a) the pristine and (b) the surface-functionalized SS coupons after different exposure periods in the *D. desulfuricans* inoculated SSMB medium. R_s = resistance of the electrolyte solution, C_{dl} = capacitance of the electrical double layer (EDL), Q_{dl} = constant phase element (CPE) of the EDL, R_{ct} = charge-transfer resistance of the EDL, Q_f = CPE of the porous surface film, R_f = resistance of the porous surface film, Q_c = CPE of the coatings, and R_{po} = pore resistance of the coatings.

observed on the SS-TiO$_2$-*g*-QP(4VP) surface are probably from the initial deposition process via waterborne mechanisms rather than from cell division because little cell growth or reproduction can be observed in Figure 6k,l. The pyridinium polycationic chains have been known to be involved in the disruption of the plasma membrane, causing the release of intracellular materials (50). The ability of the inorganic−organic hybrid coatings to inhibit bacterial adhesion and proliferation is thus ascertained.

The bactericidal activity of the hybrid inorganic−organic coatings was further supported by a comparison of the viable cell counts on different substrate surfaces as a function of the exposure time (Figure 7). For the pristine SS surface, the viable cell number increased to more than 10^5 cells/cm^2 after 3 day of exposure and increased further with the exposure time. A similar phenomenon was observed for the SS-TiO$_2$ and the SS-TiO$_2$-CTS surfaces. The number of viable cells adhered to these surfaces increased by more than 2 orders of magnitude (up to approximately 10^7 cells/cm^2) after 14 days of exposure. On the other hand, the number of viable cells adhered to the SS-TiO$_2$-*g*-QP(4VP) surface remained at less than 10^3 cells/cm^2 throughout the exposure period, indicative of a low survival rate for the attached bacteria cells and confirming the effectiveness of the grafted polycationic chains in killing *D. desulfuricans*. For metal surfaces functionalized with 4VP polymers, the bactericidal activities can be correlated with the surface concentration of positively charged pyridinium (N$^+$) cations (51).

Anticorrosion Behavior of the SS-TiO$_2$-*g*-QP(4VP) Coupons. Figure 8 shows the Tafel plots of the pristine SS and surface-functionalized coupons [including the SS-TiO$_2$,

SS-TiO$_2$-CTS, and SS-TiO$_2$-*g*-QP(4VP) coupons] after various exposure periods in the *D. desulfuricans* inoculated SSMB medium. The linear portions of anodic and cathodic curves were extrapolated to obtain the values of the Tafel slopes (b_a and b_c), corrosion potentials (E_{corr}), and corrosion current densities (i_{corr}) using procedures described previously (13). The analysis results are summarized in Table 2. For the pristine SS coupon, the corrosion potential, E_{corr}, undergoes an active shift in the negative direction with exposure time. The phenomenon is usually attributed to the anodic dissolution process in terms of the mixed potential theory (7). The enhanced dissolution rate of the pristine SS coupon upon exposure to *D. desulfuricans* is supported by the significant increase in the magnitude of corrosion current densities, i_{corr}, with exposure time (Table 2). For the surface-functionalized coupons, E_{corr} undergoes a much reduced shift in comparison with the pristine SS coupons (Table 2). The ennoblement in E_{corr} is a common phenomenon for the coupons with protective coatings in comparison with the bare metal coupons (52). Among the surface-functionalized coupons, the SS-TiO$_2$-*g*-QP(4VP) coupon exhibits the most noble E_{corr} value (Table 2). The i_{corr} values for the surface-functionalized coupons, albeit increased slightly with the exposure time, are significantly lower than that of the pristine SS coupons throughout the exposure periods. The results are indicative of the good protective property of the inorganic and hybrid coatings against biocorrosion by *D. desulfuricans*. The magnitude of i_{corr} for the SS-TiO$_2$-*g*-QP(4VP) coupon is lower by about 2.5-fold than those of the SS-TiO$_2$ and SS-TiO$_2$-CTS coupons, as well as that of the nonquaternized SS-TiO$_2$-*g*-P(4VP) coupons, throughout the exposure periods, indicative of further enhancement in the inhibitory property by the combined effects of the titanium oxide multilayers and the grafted poly(vinyl-*N*-hexylpyridinium) brushes. As a consequence, the IE of the SS-TiO$_2$-*g*-QP(4VP) coupons is always higher than those of the SS-TiO$_2$ and SS-TiO$_2$-CTS coupons. The effectiveness of the hybrid coatings in protecting the SS substrate from the synergistic attack of active Cl$^-$ anions, biogenic S^{2-}, and *D. desulfuricans* biofilms is thus ascertained.

Figure 9 shows the impedance spectra of various SS coupons after different exposure periods in the *D. desulfuricans* inoculated SSMB medium. The impedance spectra are usually analyzed by fitting with appropriate equivalent electrical circuits (EECs). The nonlinear least-squares fitting procedure, i.e., EQUIVCRT, by Boukamp was used to iteratively adjust the values of circuit elements to achieve the best match between the experimental results and the fitted data (53). Two EECs were proposed to model the respective impedance spectra of the pristine and surface-functionalized SS coupons (Figure 10). ECC(a) is used to fit the impedance spectra of the coupons with a porous surface film, while ECC(b) has been widely used to estimate the barrier and extent of protection and degradation of the protective coatings on the substrate surface (54). The pore resistance (R_{po}) represents the extent of ionic conduction through a polymer in an electrolytic environment and is commonly used as a criterion for assessing the extent of corrosion protection

Table 3. Parameters for the Fitting of Electrochemical Impedance Spectroscopy Spectra of the Pristine and Surface-Functionalized Coupons in the *D. desulfuricans* Inoculated Medium for Various Exposure Periods

					Q_{dl}			Q_f			Q_c		
samples	time (days)	R_s (Ω)	R_{ct} (kΩ)	C_{dl} (μF)	$Y_0 \times 10^{-4}$ (Ω^{-1} s^n)	n_0	R_f (kΩ)	$Y_1 \times 10^{-5}$ (Ω^{-1} s^n)	n_1	R_{po} (kΩ)	$Y_2 \times 10^{-4}$ (Ω^{-1} s^n)	n_2	$\Sigma\chi^2 \times 10^{-3}$
pristine SS[a]	3	13.22	2.01	0.48			0.25	20.98	0.72				0.49
SS-TiO$_2$[b]		12.09	4.34		1.29	0.76				5.12	12.92	0.70	1.49
SS-TiO$_2$-CTS[b]		14.29	5.34		2.46	0.75				7.44	2.58	0.74	7.98
SS-TiO$_2$-g-QP(4VP)[b]		16.66	8.89		0.61	0.77				18.64	0.73	0.79	9.73
pristine SS	14	14.59	0.50	29.91			0.93	3.04	0.84				3.27
SS-TiO$_2$		12.63	4.52		1.33	0.75				5.67	12.98	0.71	1.89
SS-TiO$_2$-CTS		13.75	4.65		2.81	0.79				6.79	3.32	0.83	5.04
SS-TiO$_2$-g-QP(4VP)		16.81	8.09		0.70	0.76				18.52	0.76	0.82	9.08
pristine SS	21	12.27	0.41	39.64			0.55	4.80	0.73				3.31
SS-TiO$_2$		12.07	4.36		1.37	0.76				4.92	14.43	0.68	1.21
SS-TiO$_2$-CTS		13.25	4.39		2.28	0.71				5.66	5.05	0.74	4.02
SS-TiO$_2$-g-QP(4VP)		14.08	7.35		0.48	0.80				16.23	0.89	0.76	1.04

[a] The impedance spectra of the pristine SS coupons are fitted with an EEC (part a in Figure 10). [b] The impedance spectra of the surface-functionalized coupons are fitted with an EEC (part b in Figure 10).

derived from the protective coatings, while the constant phase element of coating, Q_c, is used to substitute coating capacitance, C_c, by taking into account the phenomena related to the heterogeneous surface and diffusion process (55).

The fitted parameters of the impedance spectra are summarized in Table 3. The charge-transfer resistance, R_{ct}, of the pristine SS coupons decreases gradually with the exposure time, indicative of an increase in the corrosion rate under the effect of *D. desulfuricans*. For the SS-TiO$_2$ coupons, the values of R_{ct} are much larger than those of the pristine SS coupons and remain almost unchanged with the exposure time, indicative of the good anticorrosion capability of the titanium oxide multilayer coatings. In the case of the SS-TiO$_2$-g-QP(4VP) coupons, the R_{ct} values are significantly larger than those of the pristine SS coupons and the other two surface-functionalized coupons throughout the exposure period, indicating that the corrosion of the SS coupons is markedly retarded under the protection of the hybrid inorganic−organic coatings. The pore resistance, R_{po}, of the SS-TiO$_2$ coupons initially undergoes an increase in magnitude because of deposition of calcium and phosphorus associated with apatites. This phenomenon can be attributed to the bioactive property of the SS-TiO$_2$ surface, as described in the previous studies (29). The R_{po} values of the SS-TiO$_2$-g-QP(4VP) coupons are significantly larger than those of the SS-TiO$_2$ and SS-TiO$_2$-CTS coupons, indicative of the substantial increase in the barrier property of the hybrid inorganic−organic coatings against the penetration of aggressive ions and water. The coating capacitance (Q_c) as a function of the exposure time in an electrolyte solution provides information on the coating stability and water uptake (55). The Q_c values of the SS-TiO$_2$ and SS-TiO$_2$-CTS coupons increase slightly with the exposure time, indicative of the uptake of the electrolyte and water in the protective coatings. Q_c of the SS-TiO$_2$-g-QP(4VP) coupon remains constant with the exposure time, indicative of improved stability

of the inorganic−organic hybrid coatings. Therefore, tailoring of the metal surface with inorganic−organic hybrid coatings via a combination of the LBL sol−gel deposition process and surface-initiated ATRP represents an effective approach to the preparation of bactericidal and anticorrosion surfaces for combating biocorrosion.

CONCLUSIONS

A novel approach to combating biocorrosion of SS in seawater by SRB involved surface functionalization with inorganic−organic hybrid coatings. The process of preparing the hybrid coatings involved the following: (i) deposition of nanostructured titanium oxide multilayer coatings on a hydroxylated SS surface via a LBL sol−gel process, (ii) covalent immobilization of an alkyl halide ATRP initiator monolayer on the titanium oxide-coated SS surface via a chlorosilane coupling agent, (iii) functionalization of the substrate surface via surface-initiated ATRP of 4VP to produce P(4VP) brushes, (iv) quaternization of the P(4VP) brushes via N-alkylation to introduce the positively charged pyridinium nitrogen (N$^+$) moieties. Not only was the coupon with the hybrid inorganic−organic coating effective in inhibiting bacterial adhesion and proliferation, it also exhibited bactericidal effects, as revealed by the cell adhesion and viability assay. The inorganic−organic hybrid coating was found to significantly enhance the resistance of the SS substrate to biocorrosion by *D. desulfuricans* because of a combination of the protective characteristics of the titanium oxide multilayers and the biocidal effect of the QP(4VP) brushes.

REFERENCES AND NOTES

(1) Borenstein, S. *Microbiologically Influenced Corrosion Handbook*; Woodhead Publishing Ltd.: Cambridge, U.K., 1994.
(2) Costerton, J. W. In *Biofouling and Biocorrosion in Industrial Water Systems*; Fleming, H. C., Geesey, G. G., Eds.; Springer-Verlag: New York, 1991.
(3) George, R. P.; Muraleedharan, P.; Sreekumari, K. R. *Biofouling* **2003**, *19*, 1–8.
(4) Iverson, W. P. *Science* **1966**, *151*, 986–988.

(5) Hamilton, W. A.; Lee, W. C. In *Biocorrosion in sulfate reducing bacteria*; Barton, L. L., Eds.; Plenum Press: New York, 1995.

(6) Beech, I. B.; Sunner, J. *Curr. Opin. Biotechnol.* **2004**, *15*, 181–186.

(7) King, R. A.; Wakerley, D. S. *Br. Corros. J.* **1973**, *8*, 41–45.

(8) Little, B. J.; Lee, J. S. In *Microbially Influenced Corrosion*; Rovid, R. W., Eds.; John Wiley & Sons, Inc.: Hoboken, NJ, 2007; pp 237–239.

(9) Videla, H. A. *Int. Biodeterior. Biodegrad.* **2002**, *49*, 259–270.

(10) Turley, P. A.; Fenn, R. J.; Ritter, J. C.; Callow, M. E. *Biofouling* **2005**, *21*, 31–40.

(11) Yebra, D. M.; Kiil, S.; Dam-Johansen, K. *Prog. Org. Coat.* **2004**, *50*, 75–104.

(12) Al-Darbi, M. M.; Muntasser, Z. M.; Tango, M.; Islam, M. R. *Energy Sources* **2002**, *24*, 1009–1018.

(13) Yuan, S. J.; Xu, F. J.; Kang, E. T.; Pehkonen, S. O. *J. Electrochem. Soc.* **2007**, *154*, C645–C657.

(14) Majumdar, P.; Lee, E.; Patel, N.; Ward, K.; Stafslien, S. J.; Daniels, J.; Chisholm, B. J.; Boudjouk, P.; Callow, M. E.; Callow, J. A.; Thompson, S. E. M. *Biofouling* **2008**, *24*, 185–200.

(15) Akid, R.; Wang, H. M.; Smith, T. J.; Greenfield, D.; Earthman, J. C. *Adv. Funct. Mater.* **2008**, *18*, 203–211.

(16) Kawabata, N.; Nishiguchi, M. *Appl. Environ. Microbiol.* **1988**, *54*, 2532–2535.

(17) Ignatova, M.; Voccia, S.; Gilbert, B.; Markova, N.; Cossement, D.; Gouttebaron, R.; Jérôme, R.; Jérôme, C. *Langmuir* **2006**, *22*, 255–262.

(18) Voccia, S.; Ignatova, M.; Jérôme, R.; Jérôme, C. *Langmuir* **2006**, *22*, 8607–8613.

(19) Cen, L.; Neoh, K. G.; Kang, E. T. *Langmuir* **2003**, *19*, 10295–10303.

(20) Sambhy, V.; Peterson, B. R.; Sen, A. *Langmuir* **2008**, *24*, 7549–7558.

(21) Lamaka, S. V.; Montemor, M. F.; Galio, A. F.; Zheludkevich, M. L.; Trindade, C.; Dick, L. F.; Ferreira, M. G. S. *Electrochim. Acta* **2008**, *53*, 4773–4783.

(22) Zheludkevich, M. L.; Salvado, I. M.; Ferreira, M. G. S. *J. Mater. Chem.* **2005**, *15*, 5099–5111.

(23) Poznyak, S. K.; Zheludkevich, M. L.; Raps, D.; Gammel, F.; Yasakau, K. A.; Ferreira, M. G. S. *Prog. Org. Coat.* **2008**, *62*, 226–235.

(24) Atanacio, A. J.; Latella, B. A.; Barbe, C. J.; Swain, M. V. *Surf. Coat. Technol.* **2005**, *192*, 354–364.

(25) Sanchez, U.; Soler-Illa, G. J. A. A.; Ribot, F.; Mayer, C. R.; Cabuil, V.; Lalot, T. *Chem. Mater.* **2001**, *13*, 3061–3083.

(26) Schottner, G. *Chem. Mater.* **2001**, *13*, 3422–3435.

(27) Schubert, U.; Hüsing, N.; Lorenz, A. *Chem. Mater.* **1995**, *7*, 2010–2027.

(28) Pyun, J.; Matyjaszewski, K. *Chem. Mater.* **2001**, *13*, 3436–3448.

(29) Yuan, S. J.; Xu, F. J.; Pehkonen, S. O.; Ting, Y. P.; Neoh, K. G.; Kang, E. T. *J. Electrochem. Soc.* **2008**, *155*, C196–C210.

(30) Queffelec, J.; Gaynor, S. G.; Matyjaszewski, K. *Macromolecules* **2000**, *33*, 8629–8639 .

(31) Martin, H. J.; Schulz, K. H.; Bumgardner, J. D.; Walters, K. B. *Langmuir* **2007**, *23*, 6645–6651.

(32) Ichinose, I.; Senzu, H.; Kunitake, T. *Chem. Lett.* **1996**, *25*, 831–832.

(33) Wagner, C. D.; Moulder, J. F.; Davis, J. E.; Riggs, W. M. In *Handbook of X-ray Photoelectron Spectroscopy*; Perkin-Elmer Corp.: Waltham, MA, 1992; pp 40, 45, 73.

(34) Tan, K. L.; Woon, L. L.; Wong, H. K.; Kang, E. T.; Neoh, K. G. *Macromolecules* **1993**, *26*, 2832–2836.

(35) Advincula, M. C.; Petersen, D.; Rahemtulla, F.; Advincula, R.; Lemons, J. E. *J. Biomed. Mater. Res., Part B* **2007**, *80B*, 107–120.

(36) Zhang, F.; Xu, F. J.; Kang, E. T.; Neoh, K. G. *Ind. Eng. Chem. Res.* **2006**, *45*, 3067–3073.

(37) Beamson, G.; Briggs, D. *High-Resolution XPS of Organic Polymers: the Scienta ESCA 300 Database*; John Wiley: Chichester, U.K., 1992.

(38) Wang, J. S.; Matyjaszewski, K. *J. Am. Chem. Soc.* **1995**, *117*, 5614–5615.

(39) Liu, Y.; Wang, L.; Pan, C. Y. *Macromolecules* **1999**, *32*, 8301–8305.

(40) Xu, F. J.; Zhong, S. P.; Yung, L. Y. L.; Tong, Y. W.; Keng, E. T.; Neoh, K. G. *Biomaterials* **2006**, *27*, 1236–1245.

(41) Matyjaszewski, K.; Miller, P. J.; Shukla, N.; Immaraporn, B.; Gelman, A.; Luokala, B. B. *Macromolecules* **1999**, *32*, 8716–8724.

(42) Biesalski, M.; Rühe, J. *Macromolecules* **2004**, *37*, 2196–2202.

(43) Little, B. J.; Ray, R. I.; Wagner, P. A.; Jones-Meehan, J.; Lee, C. C.; Mansfeld, F. *Biofouling* **1999**, *13*, 301–321.

(44) Videla, H. A.; Wilkes, J. F. *Manual of Biocorrosion*; CRC Press Inc.: Boca Raton, FL, 1996.

(45) Costerton, J. W.; Stewart, P. S.; Greenberg, E. P. *Science* **1999**, *284*, 1318–1322.

(46) Reid, G.; Lam, D.; Policova, Z.; Neumann, A. W. *J. Mater. Sci., Mater. Med.* **1993**, *4*, 17–22.

(47) Kuhl, T. L.; Leckband, D. E.; Lasic, D. D.; Israelachvili, J. N. *Biophys. J.* **1994**, *66*, 1479–1488.

(48) Allion, A.; Baron, J. P.; Boulange-Petermann, L. *Biofouling* **2006**, *22*, 269–278.

(49) Rubio, C.; Costa, D.; Bellon-Fontaine, M. N.; Relkin, P.; Pradier, C. M.; Marcus, P. *Colloids Surf. B* **2002**, *24*, 193–205.

(50) Tiller, J. C.; Lee, S. B.; Klibanov, A. M. *Biotechnol. Bioeng.* **2002**, *79*, 465–471.

(51) Yuan, S. J.; Lu, C. K.; Pekonen, S. O.; Bai, R. B.; Neoh, K. G.; Ting, Y. P.; Kang, E. T. *Biofouling* **2009**, *25*, 109–125.

(52) Spinks, G. M.; Dominis, A. J.; Wallace, G. G.; Tallman, D. E. *J. Solid State Electrochem.* **2002**, *6*, 85–100.

(53) Boukamp, B. A. *Solid State Ionics* **1986**, *20*, 31–44.

(54) Mansfeld, F. *J. Appl. Electrochem.* **1995**, *25*, 187–202.

(55) Mansfeld, F.; Jeanjaquet, S. L.; Kendig, M. W. *Corros. Sci.* **1986**, *28*, 735–742.